Density functional theory of the electrical double layer: the RFD functional

Dirk Gillespie[1,3]**, Mónika Valiskó**[2] **and Dezső Boda**[2]

[1] Department of Molecular Biophysics and Physiology, Rush University Medical Center,
1750 West Harrison Street, Suite 1289, Chicago, IL 60612, USA
[2] Department of Physical Chemistry, University of Veszprém, PO Box 158, H-8201 Veszprém,
Hungary

E-mail: dirk_gillespie@rush.edu

Abstract
Density functional theory (DFT) of electrolytes is applied to the electrical
double layer under a wide range of conditions. The ions are charged, hard
spheres of different size and valence, and the wall creating the double layer
is uncharged, weakly charged, and strongly charged. Under all conditions,
the density and electrostatic potential profiles calculated using the recently
proposed RFD electrostatic functional (Gillespie *et al* 2002 *J. Phys.: Condens.
Matter* **14** 12129; 2003 *Phys. Rev.* E **68** 031503) compare well to Monte Carlo
simulations. When the wall is strongly charged, the RFD functional results
agree with the results of a simpler perturbative electrostatic DFT, but the two
functionals' results qualitatively disagree when the wall is uncharged or weakly
charged. The RFD functional reproduces these phenomena of weakly charged
double layers. It also reproduces bulk thermodynamic quantities calculated
from pair correlation functions.

1. Introduction

Fluids of charged, hard spheres are widely used to represent physical systems such as electrolyte
solutions, colloids, and macromolecular environments. Density functional theory (DFT)
provides a computationally inexpensive way to determine particle density profiles of these
fluids. However, DFT is an approximation, and any new DFT must be tested, both for accuracy
against MC simulations and for thermodynamic self-consistency against sum rules. This paper
aims to test a recent DFT of charged, hard spheres.

---

[3] Author to whom any correspondence should be addressed.

DFT determines thermodynamic properties of inhomogeneous fluids from the excess free energy F_{ex} and its functional dependence on the set of all the particle densities $\{\rho_k(\mathbf{y})\}$, where k is the index of one ion species:

$$F_{ex} = F_{ex}[\{\rho_k(\mathbf{y})\}]. \tag{1}$$

For uncharged, hard spheres, accurate approximations of F_{ex} derived from fundamental measure theory are available [1–4]. There are, however, few accurate approximations of F_{ex} for fluids of charged, hard spheres.

Several methods have been applied to approximate the electrostatic component of F_{ex}. These include thermodynamic integration [5, 6], the weighted density approximation [7–9], and perturbation theories. These perturbation methods expand F_{ex} in a functional Taylor series about a reference fluid that is truncated after the quadratic term. The difference between the perturbation methods is the choice of reference fluid. In the original derivations, the reference fluid is the bulk fluid that determines the chemical potentials of the ions [10, 11], but inhomogeneous reference fluids are also possible [12]. The bulk-fluid reference approach has been applied to different systems [13–17]. Another approach uses an inhomogeneous reference fluid that is itself a functional of the particle densities $\{\rho_k(\mathbf{y})\}$ [18, 19]. This new 'reference' functional (given the name 'RFD functional' to recall its origin as a 'reference fluid density' [19]) has been used in recent studies [18, 20]. To distinguish between these two perturbation approaches, we will refer to them as the bulk-fluid (BF) and RFD methods.

One of the strengths of the RFD approach is that it can be used in systems with two fluids separated by a semipermeable membrane. Depending on the conditions, the concentration of a species in the one compartment far from the membrane may be orders of magnitude larger than its concentration in the other compartment. For example, in some biological ion channels, the normal physiological range for the concentration of Ca^{2+} is seven orders of magnitude, from 1 μM to more than 10 M [18, 21]. In a system with a semipermeable membrane, on both sides of the membrane the system becomes homogeneous far from the interface; two bulk fluids with different concentrations are established although the system is inhomogeneous near the membrane. The BF method necessarily requires choosing the bulk concentrations on one side as reference concentrations. If there is a large difference between the bulk concentrations on the two sides of the membrane, the BF approach inherently involves calculating a large perturbation to the chosen reference system when, ideally, any perturbation should be small. Moreover, [19] shows that the common method [13–19] of using the mean spherical approximation (MSA) [22] to describe the reference system *cannot* calculate an accurate bulk density on the other side.

The RFD approach was originally constructed for systems with a semipermeable membrane where the density profiles are smooth. The purpose of this paper is to compare the RFD method to MC simulations of the electrical double layer (where the density profiles are discontinuous) with the goal of understanding the strengths and weaknesses of the RFD approach in reproducing the effects of ions of unequal size and charge [23]. Other DFT studies of the double layer have assumed that the ions were the same size (the restricted primitive model) [6, 7, 11, 12, 16].

We consider a wide range of conditions, with bath concentrations ranging from 0.05 to 3 M, ion diameters ranging from 0.15 to 0.425 nm, ion valences ranging from ± 1 to ± 3, and wall surface charge density ranging from 0 to ± 0.5 C m^{-2}. In all cases, the RFD approach reproduces the MC results well. Compared to the BF approach, the RFD functional results are more accurate, particularly when the wall is uncharged or weakly charged. Both functionals reproduce bulk thermodynamic quantities well and with similar accuracy.

2. Theory

2.1. Model of the system

We consider the primitive model of a binary electrolyte near a hard, planar, charged surface. The solvent is implicitly described by a dielectric constant ϵ that is uniform throughout the system. The ions are modelled as charged, hard spheres so that the interaction potential between ions of species i and j is

$$u_{ij}(r) = \begin{cases} \infty & r \leqslant d_{ij} \\ \dfrac{z_i z_j e^2}{4\pi \epsilon \epsilon_0 r} & r > d_{ij}, \end{cases} \tag{2}$$

where e is the fundamental charge, ϵ_0 is the permittivity of vacuum, r is the distance between the two ions, and z_i and d_i are the valence and diameter, respectively, of ion species i. The contact distance is

$$d_{ij} = \frac{d_i + d_j}{2}. \tag{3}$$

The ion–wall interaction potential is

$$u_i(x) = \begin{cases} \infty & x \leqslant d_i/2 \\ -\dfrac{z_i e \sigma}{2\epsilon \epsilon_0} x & x > d_i/2, \end{cases} \tag{4}$$

where σ is the surface charge density of the wall and x is the distance of the ion from the wall. In our calculations, the temperature $T = 298.15$ K and the dielectric constant $\epsilon = 78.5$.

2.2. The electrostatic functional

The electrostatic functional we use is described in detail in [18, 19]. Here, we briefly summarize it.

Perturbation methods approximate $F_{ES}[\{\rho_k(\mathbf{y})\}]$ with a functional Taylor series, truncated after the quadratic term, expanded around a reference fluid:

$$F_{ES}[\{\rho_k(\mathbf{y})\}] \approx F_{ES}[\{\rho_k^{ref}(\mathbf{y})\}] - kT \sum_i \int c_i^{(1),ES}[\{\rho_k^{ref}(\mathbf{y})\}; \mathbf{x}] \Delta\rho_i(\mathbf{x}) \, d\mathbf{x}$$
$$- \frac{kT}{2} \sum_{i,j} \int \int c_{ij}^{(2),ES}[\{\rho_k^{ref}(\mathbf{y})\}; \mathbf{x}, \mathbf{x}'] \Delta\rho_i(\mathbf{x}) \Delta\rho_j(\mathbf{x}') \, d\mathbf{x} \, d\mathbf{x}' \tag{5}$$

with

$$\Delta\rho_i(\mathbf{x}) = \rho_i(\mathbf{x}) - \rho_i^{ref}(\mathbf{x}), \tag{6}$$

where $\rho_i^{ref}(\mathbf{x})$ is a given (and possibly inhomogeneous) reference density profile. The RFD approach makes the reference fluid densities functionals of the particle densities $\rho_i(\mathbf{x})$ [19]:

$$\rho_k^{ref}(\mathbf{y}) = \bar{\rho}_k[\{\rho_i(\mathbf{x})\}; \mathbf{y}]. \tag{7}$$

$\bar{\rho}_k$ is the RFD functional, recalling its origin as a 'reference fluid density'. Reference [19] shows that the first-order direct correlation function (DCF) is given by

$$c_i^{(1),ES}(\mathbf{x}) = -\frac{1}{kT} \frac{\delta F_{ES}}{\delta \rho_i(\mathbf{x})} \tag{8}$$

$$\approx \bar{c}_i^{(1),ES}(\mathbf{x}) + \sum_j \int \bar{c}_{ij}^{(2),ES}(\mathbf{x}, \mathbf{x}') \Delta\rho_j(\mathbf{x}') \, d\mathbf{x}', \tag{9}$$

where

$$\Delta\rho_k(\mathbf{x}) = \rho_k(\mathbf{x}) - \bar{\rho}_k(\mathbf{x}), \tag{10}$$

$$\bar{c}_i^{(1),\text{ES}}(\mathbf{x}) = c_i^{(1),\text{ES}}[\{\bar{\rho}_k(\mathbf{y})\}; \mathbf{x}], \tag{11}$$

and

$$\bar{c}_{ij}^{(2),\text{ES}}(\mathbf{x}, \mathbf{x}') = c_{ij}^{(2),\text{ES}}[\{\bar{\rho}_k(\mathbf{y})\}; \mathbf{x}, \mathbf{x}']. \tag{12}$$

For the RFD functional, the densities $\bar{\rho}_k(\mathbf{x})$ must be chosen so that both the first- and second-order DCFs can be estimated. This is possible because the densities $\{\bar{\rho}_k(\mathbf{x})\}$ are a mathematical construct and do not represent a physically real fluid. The particular choice of the RFD functional we use here is that of [18], which is also discussed in [19]:

$$\bar{\rho}_i[\{\rho_k(\mathbf{x}')\}; \mathbf{x}] = \frac{3}{4\pi R_{\text{ES}}^3(\mathbf{x})} \int_{|\mathbf{x}'-\mathbf{x}| \leqslant R_{\text{ES}}(\mathbf{x})} \alpha_i(\mathbf{x}')\rho_i(\mathbf{x}') \, d\mathbf{x}', \tag{13}$$

where the $\{\alpha_k\}$ are chosen so that the fluid with densities $\{\alpha_k(\mathbf{x})\rho_k(\mathbf{x})\}$ is charge-neutral and has the same ionic strength as the fluid with densities $\{\rho_k(\mathbf{x})\}$ at every point $\mathbf{x}$. The radius of the sphere $R_{\text{ES}}(\mathbf{x})$ over which we average is the local electrostatic length scale. Specific formulae for $\alpha_k(\mathbf{x})$ and $R_{\text{ES}}(\mathbf{x})$ are given in [18, 19]. To estimate the electrostatic DCFs $\bar{c}_i^{(1),\text{ES}}(\mathbf{x})$ and $\bar{c}_{ij}^{(2),\text{ES}}(\mathbf{x}, \mathbf{x}')$ at each point, we use a bulk formulation (specifically the MSA) at each point $\mathbf{x}$ with densities $\bar{\rho}_k(\mathbf{x})$ [22, 24, 25].

This RFD functional has also been used by Sokołowski *et al* to create a (nonperturbative) weighted density approximation electrostatic functional [8, 9]. They applied the energy route of the MSA to define F_{ES} as a functional only of the $\{\bar{\rho}_k(\mathbf{x})\}$. Their approach successfully described the phase behaviour of the restricted primitive model (RPM) of electrolytes in pores [8] and the anomalous temperature dependence of the capacitance of the electrical double layer of the RPM [9].

By defining RFD densities to be the bulk densities, the BF perturbation method is recovered.

2.3. Numerical implementation of the double layer with DFT

We model the wall approximately as a semipermeable membrane with a neglible permeability to all the ions in the system. We do this because of the RFD functional approach. The RFD densities $\{\bar{\rho}_k(\mathbf{x})\}$ are nonlocal averages of the densities $\{\rho_k(\mathbf{x})\}$ (equation (13)). Therefore, while $\rho_k(\mathbf{x}) = 0$ for all ion species k immediately behind the wall, the RFD densities $\{\bar{\rho}_k(\mathbf{x})\}$ are *not* zero behind the wall because of the convolution integral in equation (13). The values of these functions behind the wall affect the ion concentrations $\{\rho_k(\mathbf{x})\}$ in front of the wall through the convolution integral in equation (9). By modelling the wall as a semipermeable membrane, it is straightforward to compute the convolutions in equations (9) and (13).

The negligible ion concentrations behind the wall are established by giving all ions a large penalty μ_{wall} for moving behind the wall. We used values between 23 and 30 kT for μ_{wall} because for these values the ion concentrations in the left bath are negligible, but still larger than machine precision:

$$\rho_i(x < d_i/2) \propto \exp\left(-\frac{\mu_{\text{wall}}}{kT}\right) = e^{-23} \approx 10^{-10}, \tag{14}$$

where the ions are excluded from $x \leqslant 0$. In the numerical implementation, the results did not depend on the exact value of μ_{wall}.

In any system with a semipermeable membrane, two bulk fluids are established far from the membrane. In our case, the right bath ($x > 0$) determines the chemical potential μ_i of

each ion species i by the bulk densities $\{\rho_k^R\}$ and by assuming that the right bath has zero electrostatic potential. The bulk concentrations $\{\rho_k^L\}$ far to the left of the membrane ($x < 0$) can be directly calculated because this bath is in equilibrium with the right bath:

$$\rho_i^L = \exp\left(\frac{\mu_i}{kT} - \frac{z_i e}{kT} V - \frac{\mu_{\text{wall}}}{kT}\right). \tag{15}$$

Because the ion concentrations are negligible to the left of the wall, equation (15) assumes that the excess chemical potentials in the left bath are zero. For a general semipermeable membrane, the excess chemical potential for the densities $\{\rho_k^L\}$ must be included as well.

V is the Donnan potential of the semipermeable membrane and is calculated from the charge neutrality of the left bath: $\sum_i \rho_i^L = 0$. The Donnan potential is the electrostatic potential difference between the two homogeneous fluids formed on each side of *any* semipermeable membrane (far from the membrane), whether μ_{wall} is large or small or whether μ_{wall} affects all particle species or just some [27, 28]. An equivalent description is that V is the electrostatic potential that must be applied by an electrode a long (but finite) distance away from the membrane to keep the semipermeable membrane system in equilibrium.

In our calculations we applied these values for $\{\rho_k^L\}$ and V as boundary conditions on the left-hand side of the system at $x = -1$ μm. The concentrations $\{\rho_k^R\}$ and zero electrostatic potential were imposed as boundary conditions at $x = 1$ μm. (1 μm is more than 2300 times the largest ion diameters we use.) To ensure that we placed the two electrodes far enough from the membrane, in some calculations we increased the system length to 20 μm (from 2 μm) and found the calculated results to be identical to several significant figures.

The equations are solved on a nonuniform grid. From 1 nm behind the wall to 2 nm in front of the wall (-1 nm $\leqslant x \leqslant 2$ nm) the grid is uniformly spaced at $\Delta x = 0.005$ nm. Outside this region, the grid points are spaced farther apart, with the interval increasing with distance from the edges of the uniformly spaced region [18]. Other choices of Δx did not substantially affect the results.

The surface charge σ is incorporated into the calculation by converting it into a volume charge that is placed in one interval with molar concentration $\sigma/1000 N_A \Delta x$, where N_A is Avogadro's number. This volume charge is included in the Poisson equation used to compute the mean electrostatic potential.

Details of the discretization of the equations and method of solution are given in [18].

2.4. Numerical implementation of the MC simulations

For the MC simulations, we use the canonical (constant NVT) ensemble in a simulation cell with periodic boundary conditions in the directions parallel to the double layer wall. In the perpendicular direction, the cell is confined by a uniformly charged double-layer wall on the left and by a neutral hard wall on the right, spaced far enough apart for a homogenous fluid to exist in the middle of the cell. This length of the cell varied between 8 and 23.5 nm, depending on the desired bulk ion concentration. In the other directions, the width of the cell varied between 4.5 and 12 nm. The number of particles was 300–500, depending on cell size and desired bath concentration. Very long simulations (1–2 million MC cycles) were required because of the small effects at the surface at zero electrode charge and because of association effects in simulations containing ions with high valence. The equations for the integration of the electrostatic potential profiles from the density profiles are given in [23].

We included several equivalent simulations as a check that all the programs gave the same answer in these cases. For example, simulations 13 and 15 (table 1) are equivalent because interchanging the ion labels in simulation 13 gives simulation 15—except that the ions' valences have opposite sign. When the wall is uncharged, the resulting concentration

Table 1. Table listing the parameters of the MC simulations we consider in this paper. The simulations (Sim.) are numbered from 1 to 21. The other columns are: the cation and anion valences, z_+ and z_-; the cation and anion diameters in nm, d_+ and d_-; the surface charge σ on the wall in C m^{-2}; the cation bath concentration c_+ in molar (moles l^{-1}); electrostatic potential ψ at the wall in kT/e from MC simulations and BF and RFD DFT calculations; βP, the left-hand side of equation (16); the right-hand side of equation (16), the contact sum rule (CSR), in m$^{-3} \times 10^{-27}$, from BF and RFD DFT calculations.

Sim.	z_+	z_-	d_+	d_-	σ	c_+	ψ_{MC}	ψ_{BF}	ψ_{RFD}	βP	BF CSR	RFD CSR
1	1	−1	0.2	0.425	−0.0075	1	−0.0126	0.0221	−0.0311	1.13	1.32	1.16
2	1	−1	0.2	0.425	0	1	0.169	0.195	0.146	1.13	1.32	1.16
3	1	−1	0.2	0.425	0.005	1	0.280	0.311	0.266	1.13	1.32	1.17
4	2	−1	0.15	0.425	0	0.5	0.0215	0.195	−0.0229	0.612	0.978	0.682
5	2	−1	0.3	0.425	0	0.5	−0.0350	0.0915	−0.0204	0.733	1.01	0.795
6	2	−1	0.4	0.425	0	0.5	−0.0854	0.0157	−0.0507	0.799	1.04	0.857
7	2	−1	0.2	0.425	0	0.05	−0.00341	0.0468	−0.00223	0.0730	0.0911	0.0764
8	2	−1	0.2	0.425	0.005	0.05	0.298	0.312	0.268	0.0730	0.0910	0.0763
9	2	−1	0.2	0.425	−0.005	0.05	−0.258	−0.199	−0.240	0.0730	0.0911	0.0764
10	2	−1	0.2	0.425	0	0.5	0.00528	0.162	−0.0121	0.658	0.987	0.725
11	2	−1	0.2	0.425	0.01	0.5	0.241	0.365	0.198	0.658	0.987	0.732
12	2	−1	0.2	0.425	−0.01	0.5	−0.200	−0.0297	−0.201	0.658	0.987	0.719
13	1	−2	0.2	0.425	0	2	0.299	0.257	0.221	1.38	1.98	1.52
14	2	−1	0.2	0.425	0	1	0.00497	0.242	−0.00439	1.44	2.17	1.60
15	2	−1	0.425	0.2	0	1	−0.301	−0.257	−0.221	1.38	1.98	1.52
16	1	−3	0.2	0.425	0	3	0.474	0.307	0.285	1.45	2.66	1.80
17	3	−1	0.2	0.425	0	1	−0.291	0.278	−0.268	1.52	3.20	1.98
18	3	−1	0.425	0.2	0	1	−0.474	−0.307	−0.285	1.45	2.66	1.80
19	1	−1	0.2	0.425	−0.5	1	−5.92	−5.97	−5.60	1.13	1.26	1.28
20	2	−1	0.2	0.425	−0.5	0.5	−2.91	−3.58	−2.35	1.13	1.24	1.49
21	1	−1	0.2	0.425	0.5	1	10.6	9.87	10.2	0.658	0.848	0.856

profiles for the two simulations are identical and the electrostatic potential profiles are opposite in sign. Simulations 16 and 18 are also equivalent in this sense.

Details of the MC simulation methods are given in [23, 29].

3. Results and discussion

Table 1 lists the parameters for the MC simulations and DFT calculations we consider in this paper. Except for figures 9 and 12, we show the results of a representative sample.

3.1. Structure of the double layer

We start by comparing the DFT calculations of ion profiles near an uncharged wall to MC simulations. Figures 1–3 show the concentration profiles of ions near the wall when the bulk cation concentration c_+ is 1 M and the cation valence z_+ is 1, 2, or 3. The particle diameters are $d_+ = 0.2$ nm and $d_- = 0.425$ nm. (All the ion diameters we chose are standard ion sizes used in simulations (for example, [23, 30]) and are the approximate size of ions [31].) In the MC simulations for all three cases (symbols), the cation concentrations at the wall are less than bulk, with cation depletion increasing as z_+ increases. Anions, on the other hand, are adsorbed at the wall when $z_+ = 1$ and 2 and slightly repelled when $z_+ = 3$. The concentration profiles also exhibit extrema when $z_+ = 2$ and 3; when $z_+ = 1$, the profiles are monotonic (for a discussion, see [23]). At low bath concentrations, the profiles are also monotonic, as shown
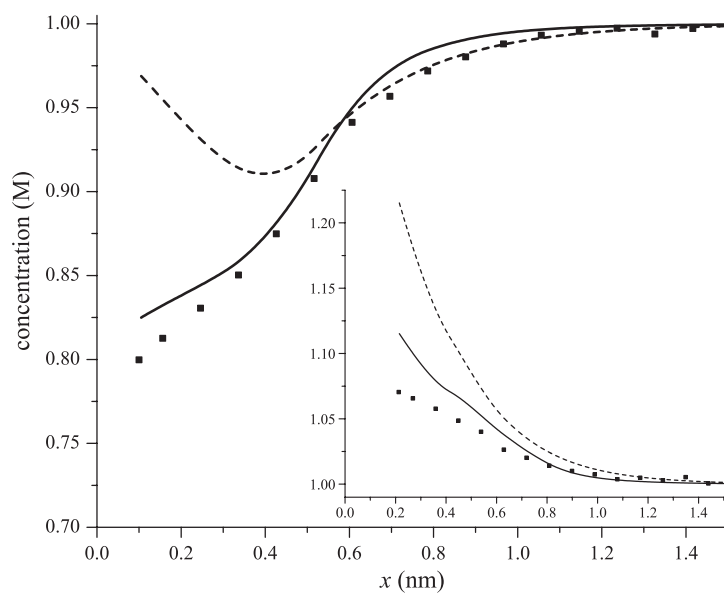
Figure 1. Comparing DFT ion concentrations of simulation 2 (table 1) to MC simulations (symbols). The wall is uncharged, the cation concentration $c_+ = 1$ M, and the ions have valence $z_+ = 1$ and $z_- = -1$. The RFD DFT is shown with the solid line and the BF DFT with the dashed line. The main figure shows the cation density profiles and the inset shows the anion concentration profiles.
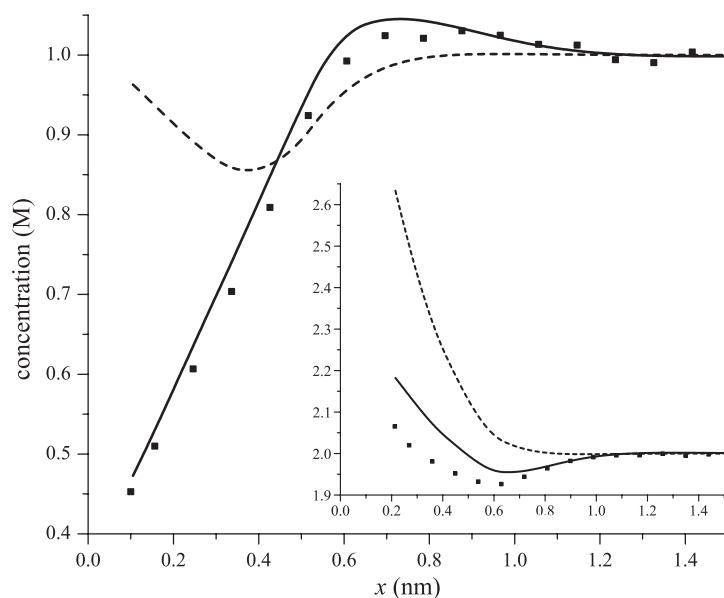

Figure 2. Comparing DFT ion concentrations of simulation 14 (table 1) to MC simulations. The system is the same as in figure 1 except that the cation charge is $z_+ = 2$. The lines, symbols, and inset are as in figure 1.

in figure 4 (symbols) with $z_+ = 2$ and $c_+ = 0.05$ M. In this case, the anions are also depleted near the wall. At high bath concentration ($c_+ = 1$ M), when the cation and anion diameters are
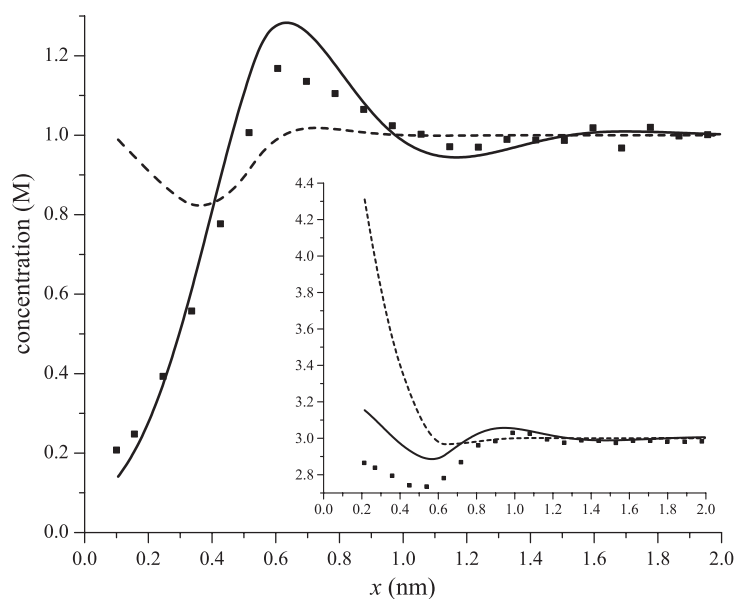
Figure 3. Comparing DFT ion concentrations of simulation 17 (table 1) to MC simulations. The system is the same as in figures 1 and 2 except that the cation charge is $z_+ = 3$. The lines, symbols, and inset are as in figure 1.
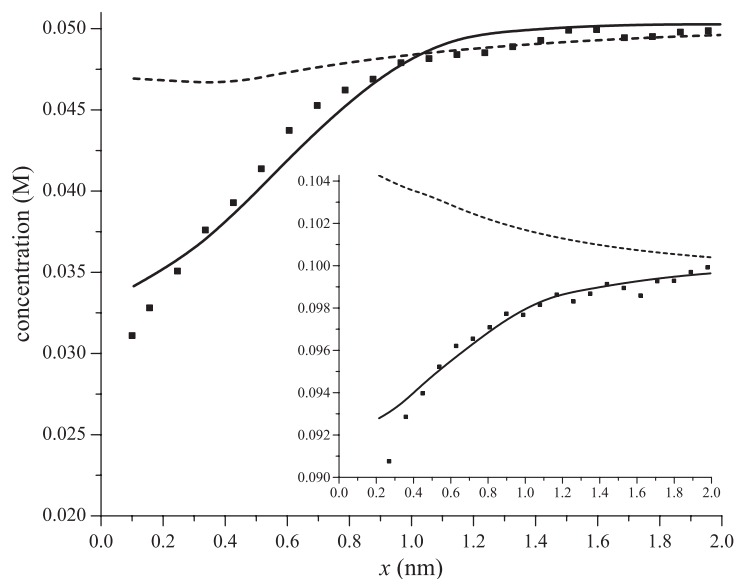

Figure 4. Comparing DFT ion concentrations of simulation 7 (table 1) to MC simulations. The system is the same as in figure 2 except that the bulk cation concentration is decreased to $c_+ = 0.05$ M from $c_+ = 1$ M. The lines, symbols, and inset are as in figure 1.

exchanged so that the cations are larger than the anions ($d_+ = 0.425$ nm and $d_- = 0.2$ nm), both anions and cations are depleted at the wall (figures 5 and 6, symbols).

All of these properties are reproduced by the RFD DFT, in most cases quantitatively (figures 1–4, solid lines), but always qualitatively (figures 5 and 6, solid lines). Comparisons
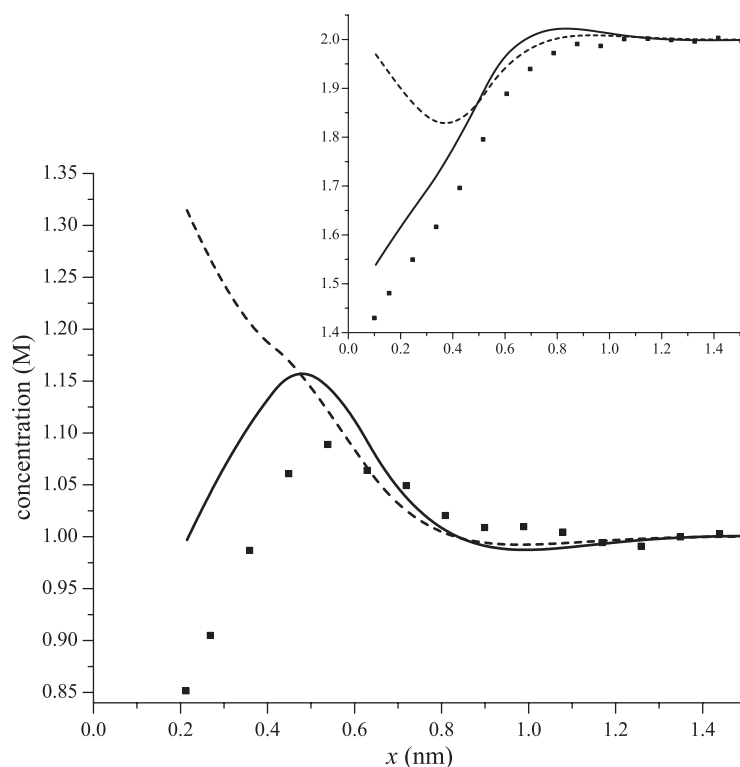
Figure 5. Comparing DFT ion concentrations of simulation 15 (table 1) to MC simulations. The system is the same as in figure 2 except that the cation and anion diameters have been exchanged to be $d_+ = 0.425$ nm and $d_- = 0.2$ nm. The lines, symbols, and inset are as in figure 1.

to other simulation data (table 1) are similar. The BF DFT, however, does not agree as well with the MC data at an uncharged wall. In general, the contact concentration calculated for the small ion is approximately the bulk concentration while the contact concentration for the large ion is greater than the bulk concentration (figures 1–6, dashed lines). This also holds at walls with small, rather than zero, surface charge density (not shown).

At a strongly charged wall, however, the two DFT methods give very similar results. For ions with $z_+ = 1$ and $z_- = -1$ at a wall with surface charge density $\sigma = -0.5$ C m^{-2} the calculated contact concentrations of both methods are nearly identical (figure 7). When $z_+ = 2$ (figure 8), the cation contact concentrations are again nearly identical, but only the RFD functional reproduces the structure of the anions.

3.2. Electrostatic potential

At equilibrium, ions of different size or valence at a hard wall create a nonzero electrostatic potential ψ at the wall [30, 32–34]. As well as being an important property of the double layer, ψ can also serve as a measure of accuracy for an approximate theory like DFT. This potential is listed in table 1 for both the MC simulations and the DFT calculations we performed. Moreover, to give an overview of the accuracy of the DFT we also graph these results in figure 9. For uncharged and weakly charged walls, the RFD functional results agree well with the MC simulation results while the BF functional results are less consistently close to the MC results (figure 9(A)).
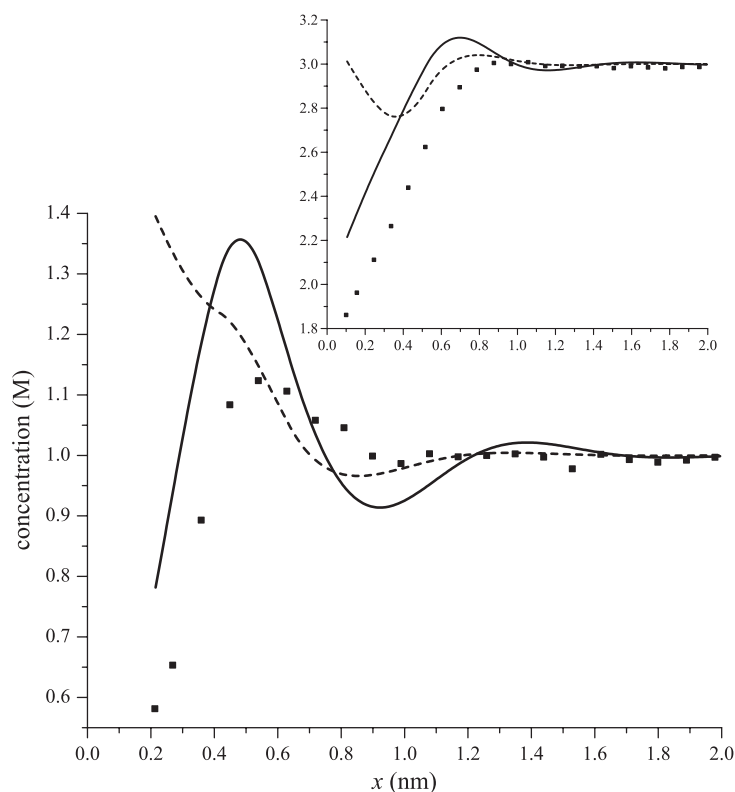
Figure 6. Comparing DFT ion concentrations of simulation 18 (table 1) to MC simulations. The system is the same as in figure 3 except that the cation and anion diameters have been exchanged to be $d_+ = 0.425$ nm and $d_- = 0.2$ nm. The lines, symbols, and inset are as in figure 1.

As with the ion concentration profiles, the BF approach agrees better with the MC results when the wall is strongly charged than when the wall is uncharged or weakly charged (figure 9(B)). At the strongly charged wall, ψ is sensitive to whether the counter-ion is the small or the large ion, an asymmetry described by Valleau and Torrie [30]. Both DFT methods reproduce this result as σ is changed from -0.5 to 0.5 C m^{-2} (simulations 19 and 21, table 1).

When the wall is strongly charged, the double layer is dominated by the counter-ions. But, when the wall is weakly charged, the co-ions also play a significant role in determining ψ. Theories of the double layer like the MSA and Gouy–Chapman fail to reproduce MC results of the dependence of ψ on ion valences or on the wall surface charge density σ [23, e.g., figures 5 and 6]. The RFD functional, however, does reproduce these results, usually quantitatively, but always qualitatively (table 1):

(1) The dependence of ψ on the valence ratio $|z_+/z_-|$ is shown in figure 10(A). When $|z_+/z_-| \geqslant 1$, the RFD results agree very well with the MC simulations, but the agreement is only qualitative when $|z_+/z_-| < 1$.
(2) The dependence of ψ on the wall surface charge density σ is shown in figure 10(B). The corresponding electrostatic potential profiles near the wall are shown in figure 11.

To our knowledge, the RFD functional is the first electrostatic DFT to reproduce these phenomena. Although not shown in this paper, the RFD functional also reproduces diameter and concentration dependencies described by Valiskó *et al* [23].
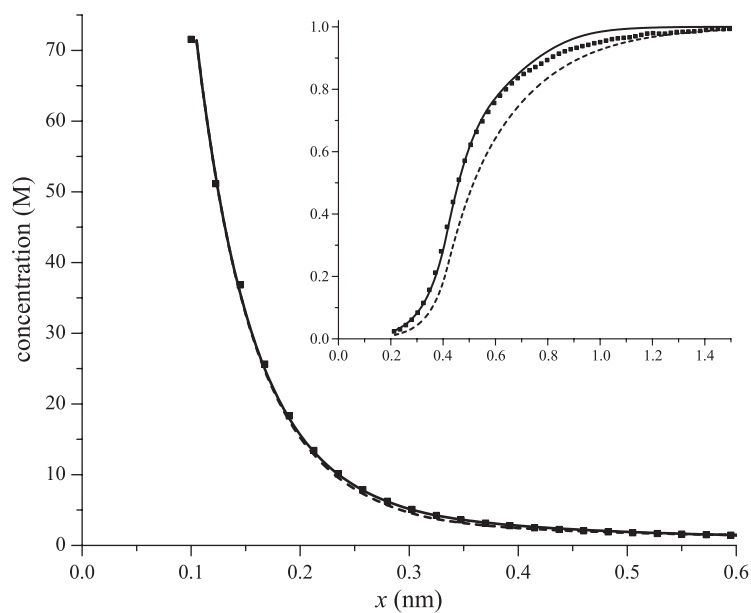
Figure 7. Comparing DFT ion concentrations of simulation 19 (table 1) to MC simulations. The wall has a surface charge of -0.5 C m^{-2} and the ions have valence $z_+ = 1$ and $z_- = -1$. The lines, symbols, and inset are as in figure 1.
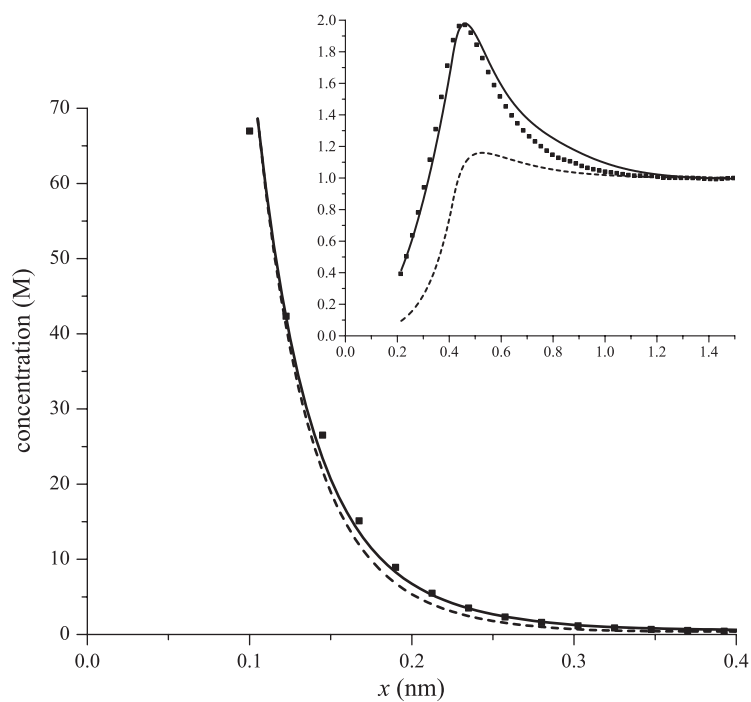

Figure 8. Comparing DFT ion concentrations of simulation 20 (table 1) to MC simulations. The wall has a surface charge of -0.5 C m^{-2} and the ions have valence $z_+ = 2$ and $z_- = -1$. The lines, symbols, and inset are as in figure 1.
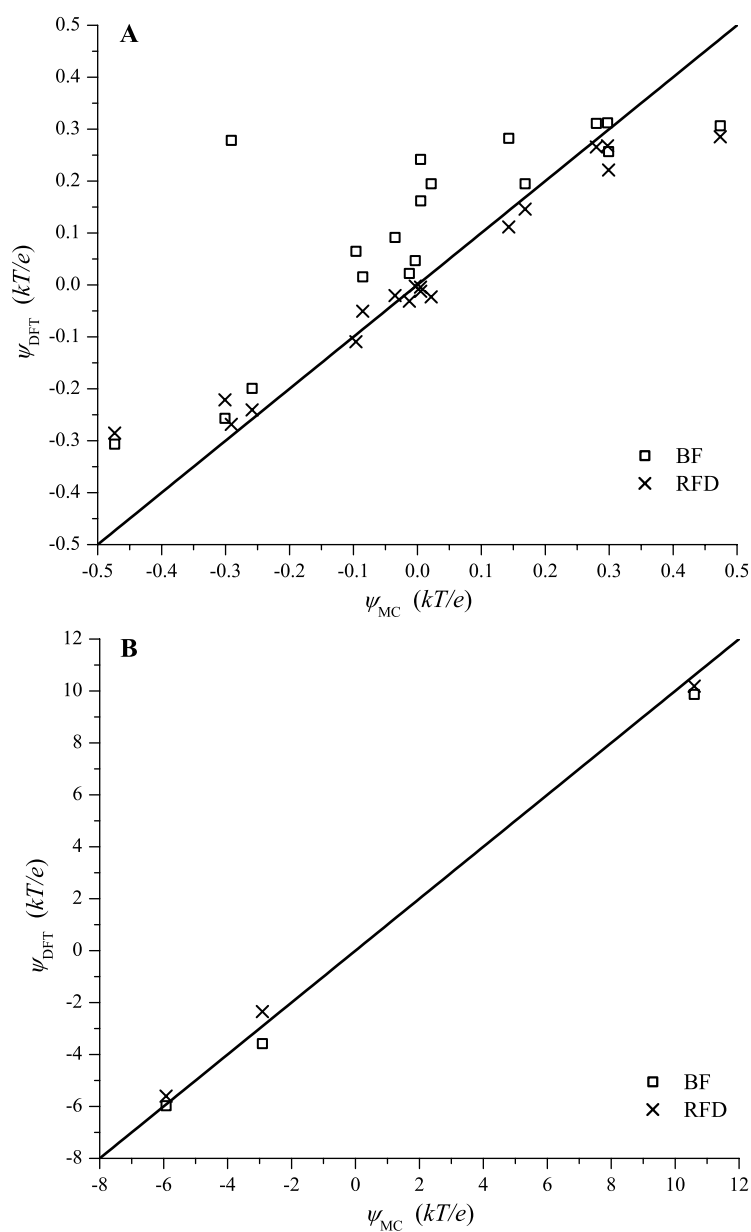
Figure 9. Comparing DFT calculations of the electrostatic potential at the wall ψ (*y*-axis) to the potential calculated from all the MC simulations listed in table 1 (*x*-axis). Exact equality is given by the line $y = x$. (A) Results of simulations 1–18 (table 1), where the wall has low or zero surface charge density. (B) Results of simulations 19–21 (table 1), where the wall has high surface charge density.

3.3. Thermodynamic self-consistency

While one measure of accuracy for a DFT is reproducing MC results, it is also important to know if a functional is thermodynamically self-consistent. There are various thermodynamic
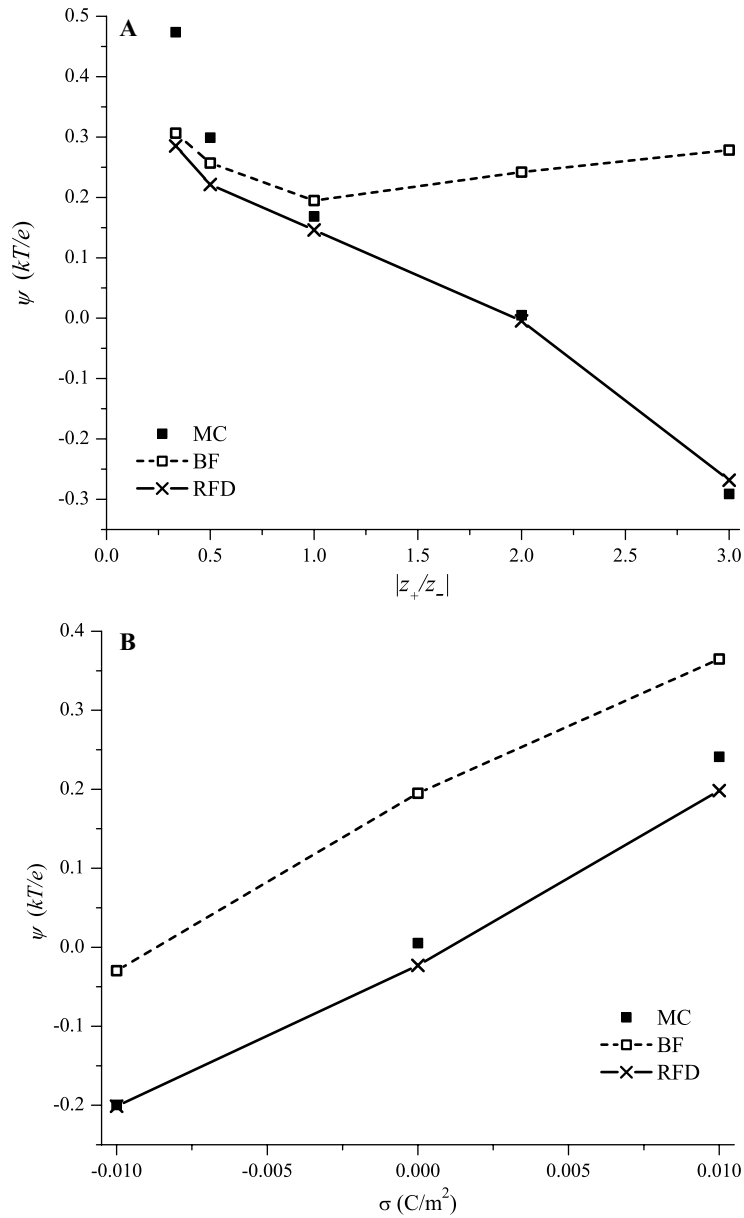
Figure 10. (A) Changes in the electrostatic potential at the wall ψ as the ratio of cation to anion valence is changed. Results from simulations 2, 13, 14, 16, and 17 (table 1) are shown. In these simulations $d_+ = 0.2$ nm and $d_- = 0.425$ nm and the ion with the largest absolute valence is at 1 M bath concentration. (B) Changes in the electrostatic potential at the wall ψ as the surface charge density σ is changed. Results from simulations 10, 11, and 12 (table 1) are shown. In these simulations $z_+ = 2$ and $z_- = -1$ and $c_+ = 0.5$ M.

sum rules of ionic fluids that can be used to test self-consistency [35]. Here we consider the contact density sum rule [35, 36]

$$\beta P = \sum_i \rho_i(d_i/2) - \frac{\beta\sigma^2}{2\epsilon\epsilon_0}, \tag{16}$$
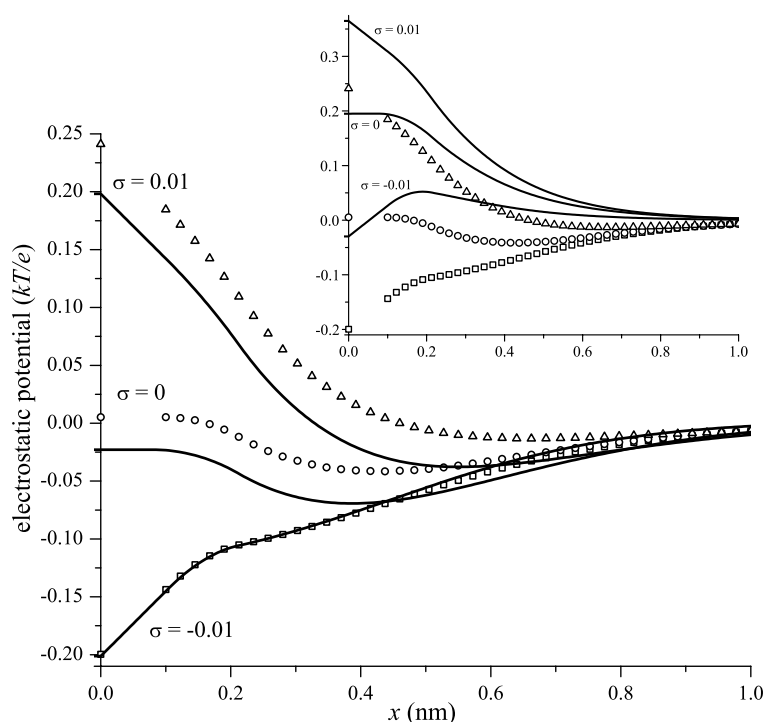
Figure 11. Comparing DFT electrostatic potential profiles (lines) of simulations 10, 11, and 12 (table 1) to MC simulations (symbols) as the wall charge density σ is changed. The main figure shows the RFD DFT results and the inset show the BF DFT results. Values of ψ for these simulations are shown in figure 10(B).

where P is the pressure of the bulk fluid far from the wall and $\beta = (kT)^{-1}$. The pressure is $P = P_{HS} + P_{ES}$, where P_{HS} is the pressure of a pure hard-sphere fluid and P_{ES} is the electrostatic component of the excess pressure. P is the same for both the BF and RFD DFTs because they use the same bulk thermodynamics. The hard-sphere component is the Percus–Yevick (compressibility) pressure ([37] and references therein). The electrostatic component uses DCFs derived from the energy route and we use the excess pressure derived from this route [38].

Figure 12 shows that both the BF and RFD functionals are not self-consistent. This has been described for the BF functional [15], but this has not been studied for the RFD functional. One reason for the inconsistency of the two functionals is a previously described shortcoming of both the BF and RFD functionals [18]: the second-order DCF from the MSA used in equation (9) cannot accurately predict the chemical potential of a bulk fluid as a perturbation of a different bulk fluid. This is because the MSA second-order DCF is thermodynamically inconsistent with the free energy of the reference fluid. Since each of these components is related to one side of the contact sum rule, the sum rule cannot be satisfied. In particular, when all ions are the same size and the MSA second-order DCF is used, the perturbation term in equation (9) is identically zero, resulting in density profiles identical to a hard-sphere fluid. On the other hand, the pressures of charged and uncharged hard-sphere fluids are obviously different. This use of an insufficiently accurate second-order DCF is (at least partly) responsible for the thermodynamic inconsistency we find. For the BF approach, Rosenfeld describes a numerical method to achieve self-consistency by calculating a better second-order DCF [11].
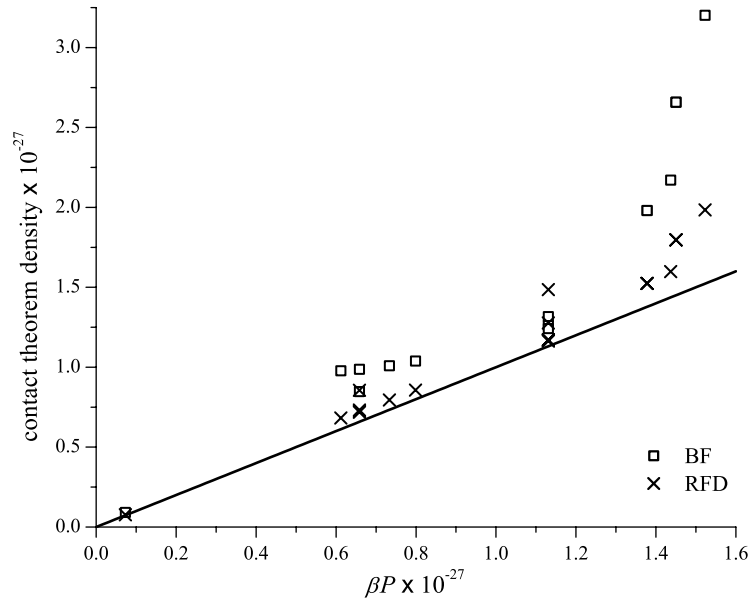
Figure 12. Testing thermodynamic self-consistency with the contact density sum rule, equation (16), for all the simulations listed in table 1. The x-axis is the left-hand side of equation (16) and the y-axis is the right-hand side. Exact equality is given by the line $y = x$. The units on both axes are m^{-3} scaled to order 1 by 10^{27}.

Both the left- and right-hand sides of equation (16) are listed in table 1. Comparing these values for the BF and RFD approaches shows that the RFD functional is almost always closer to self-consistency than the BF functional (see also figure 12). Since both P and σ are the same for both approaches, we conclude that the contact densities computed with the RFD functional are closer to the self-consistent contact densities.

3.4. Thermodynamic quantities

So far we have shown that the ion densities near the wall are well described by the RFD functional. However, there are functionals that reproduce ion structure but fail to reproduce thermodynamic quantities. To test the thermodynamic accuracy of the RFD functional we follow Li and Wu [17] and calculate the excess internal energy per particle E_{ex} and the osmotic coefficient ϕ of various bulk fluids via the pair correlation function $g_{ij}(r)$:

$$E_{ex} = \frac{2\pi}{\rho_t} \sum_{i,j} \rho_i \rho_j \int r^2 g_{ij}(r) u_{ij}(r) \, \mathrm{d}r \tag{17}$$

$$\phi = 1 + \frac{\beta E_{ex}}{3} + \frac{2\pi}{3\rho_t} \sum_{i,j} \rho_i \rho_j d_{ij}^3 g_{ij}(d_{ij}), \tag{18}$$

where ion species i has bulk density ρ_i and ρ_t is the total bulk density. In the DFT calculations, $g_{ij}(r)$ was determined by placing an ion of species j at the centre ($r = 0$) so that ion species i is subject to an external potential of $u_{ij}(r)$. The DFT equations were then solved in spherical coordinates.

The results for four bulk fluids are summarized in tables 2–5. In each case, both DFT methods reproduced the thermodynamic quantities well and with approximately the same

Table 2. Results for a bulk system with cation concentration $c_+ = 0.1$ M. The ions have valence $z_+ = 1$ and $z_- = -1$ and diameters $d_+ = 0.2$ nm and $d_- = 0.425$ nm. The first four columns show contact values for the pair correlation functions $g_{ij}(r)$. The last two columns show two bulk thermodynamic quantities, the excess internal energy per particle E_{ex} and the osmotic coefficient ϕ, calculated from the integrated pair correlation functions.

Method	$g_{++}(d_{++})$	$g_{+-}(d_{+-})$	$g_{-+}(d_{-+})$	$g_{--}(d_{--})$	βE_{ex}	ϕ
MC	0.0561	5.51	5.51	0.333	−0.279	0.930
BF	0.0496	5.85	5.60	0.317	−0.303	0.923
RFD	0.0501	5.52	5.66	0.319	−0.304	0.922

Table 3. Results for a bulk system with cation concentration $c_+ = 1$ M. The ions have valence $z_+ = 1$ and $z_- = -1$ and diameters $d_+ = 0.2$ nm and $d_- = 0.425$ nm. The first four columns show contact values for the pair correlation functions $g_{ij}(r)$. The last two columns show two bulk thermodynamic quantities, the excess internal energy per particle E_{ex} and the osmotic coefficient ϕ, calculated from the integrated pair correlation functions.

Method	$g_{++}(d_{++})$	$g_{+-}(d_{+-})$	$g_{-+}(d_{-+})$	$g_{--}(d_{--})$	βE_{ex}	ϕ
MC	0.0941	3.28	3.28	0.557	−0.605	0.154
BF	0.0952	3.39	3.32	0.534	−0.633	0.155
RFD	0.0947	3.38	3.26	0.528	−0.631	0.154

Table 4. Results for a bulk system with cation concentration $c_+ = 0.1$ M. The ions have valence $z_+ = 2$ and $z_- = -1$ and diameters $d_+ = 0.2$ nm and $d_- = 0.425$ nm. The first four columns show contact values for the pair correlation functions $g_{ij}(r)$. The last two columns show two bulk thermodynamic quantities, the excess internal energy per particle E_{ex} and the osmotic coefficient ϕ, calculated from the integrated pair correlation functions. ∗ indicates that the concentration cannot be determined because it is less than the statistical error of the MC simulation.

Method	$g_{++}(d_{++})$	$g_{+-}(d_{+-})$	$g_{-+}(d_{-+})$	$g_{--}(d_{--})$	βE_{ex}	ϕ
MC	0∗	23.3	23.3	0.825	−1.13	0.753
BF	1.47×10^{-5}	19.7	15.0	0.423	−0.924	0.787
RFD	1.63×10^{-5}	19.7	24.1	0.566	−1.01	0.783

Table 5. Results for a bulk system with cation concentration $c_+ = 1$ M. The ions have valence $z_+ = 2$ and $z_- = -1$ and diameters $d_+ = 0.2$ nm and $d_- = 0.425$ nm. The first four columns show contact values for the pair correlation functions $g_{ij}(r)$. The last two columns show two bulk thermodynamic quantities, the excess internal energy per particle E_{ex} and the osmotic coefficient ϕ, calculated from the integrated pair correlation functions.

Method	$g_{++}(d_{++})$	$g_{+-}(d_{+-})$	$g_{-+}(d_{-+})$	$g_{--}(d_{--})$	βE_{ex}	ϕ
MC	1.42×10^{-4}	5.64	5.64	0.810	−1.61	0.857
BF	1.97×10^{-4}	6.33	5.28	0.730	−1.61	0.855
RFD	1.27×10^{-4}	6.18	5.45	0.768	−1.65	0.848

accuracy. Again both DFT methods were thermodynamically inconsistent with $g_{+-}(d_{+-}) \neq g_{-+}(d_{-+})$ and again the RFD functional is closer to self-consistency.

4. Conclusion

We have shown that the RFD functional approach to computing the electrostatic functional of DFT accurately approximates the double layer structure near a charged or uncharged wall under a wide variety of conditions (table 1). The analysis also shows that functionals like the

BF functional may be more accurate the larger the wall surface charge density. Electrostatic functionals are almost exclusively compared against MC simulations with large wall surface charge density ($|\sigma| \geqslant 0.1$ C m^{-2}) [6, 7, 10, 16], but comparisons against simulations with no surface charge are also necessary.

Acknowledgments

References

[1] Rosenfeld Y 1989 *Phys. Rev. Lett.* **63** 980
[2] Rosenfeld Y, Schmidt M, Löwen H and Tarazona P 1997 *Phys. Rev.* E **55** 4245
[3] Roth R, Evans R, Lang A and Kahl G 2002 *J. Phys.: Condens. Matter* **14** 12063
[4] Yu Y-X and Wu J 2002 *J. Chem. Phys.* **117** 10156
[5] Groot R D 1988 *Phys. Rev.* A **37** 3456
[6] Mier-y-Teran L, Suh S H, White H S and Davis H T 1990 *J. Chem. Phys.* **92** 5087
    Tang Z, Scriven L E and Davis H T 1992 *J. Chem. Phys.* **97** 494
    Tang Z, Scriven L E and Davis H T 1992 *J. Chem. Phys.* **97** 9258
    Tang Z, Scriven L E and Davis H T 1994 *J. Chem. Phys.* **100** 4527
[7] Patra C N and Ghosh S K 1993 *Phys. Rev.* E **47** 4088
    Patra C N 1999 *J. Chem. Phys.* **111** 9832
    Patra C N and Ghosh S K 2002 *J. Chem. Phys.* **117** 8938
[8] Pizio O, Patrykiejew A and Sokołowski S 2004 *J. Chem. Phys.* **121** 11957
    Pizio O, Patrykiejew A and Sokołowski S 2004 *Cond. Matter Phys.* **7** 779
    Pizio O and Sokołowski S 2005 *J. Chem. Phys.* **122** 144707
[9] Reszko-Zygmunt J, Sokołowski S, Henderson D and Boda D 2005 *J. Chem. Phys.* **122** 084504
[10] Kierlik E and Rosinberg M L 1991 *Phys. Rev.* A **44** 5025
[11] Rosenfeld Y 1993 *J. Chem. Phys.* **98** 8126
[12] Patra C N and Ghosh S K 1994 *J. Chem. Phys.* **100** 5219
[13] Biben T, Hansen J-P and Rosenfeld Y 1998 *Phys. Rev.* E **57** R3727
[14] Boda D, Henderson D, Rowley R and Sokołowski S 1999 *J. Chem. Phys.* **111** 9382
    Boda D, Henderson D, Patrykiejew A and Sokołowski S 2000 *J. Chem. Phys.* **113** 802
    Henderson D, Bryk P, Sokołowski S and Wasan D T 2000 *Phys. Rev.* E **61** 3896
[15] Boda D, Fawcett W R, Henderson D and Sokołowski S 2002 *J. Chem. Phys.* **116** 7170
[16] Yu Y-X, Wu J and Gao G-H 2004 *J. Chem. Phys.* **120** 7223
[17] Li Z and Wu J 2004 *Phys. Rev.* E **70** 031109
[18] Gillespie D, Nonner W and Eisenberg R S 2002 *J. Phys.: Condens. Matter* **14** 12129
[19] Gillespie D, Nonner W and Eisenberg R S 2003 *Phys. Rev.* E **68** 031503
[20] Reszko-Zygmunt J and Sokołowski S 2004 *Cond. Matter Phys.* **7** 793
    Reszko-Zygmunt J and Sokołowski S 2005 *J. Electroanal. Chem.* **575** 249
[21] Nonner W, Catacuzzeno L and Eisenberg B 2000 *Biophys. J.* **79** 1976
    Nonner W, Gillespie D, Henderson D and Eisenberg B 2001 *J. Phys. Chem.* B **105** 6427
    Gillespie D, Xu L, Wang Y and Meissner G 2005 *J. Phys. Chem.* B **109** 15598
[22] Waisman E and Lebowitz J L 1970 *J. Chem. Phys.* **52** 4307
    Waisman E and Lebowitz J L 1972 *J. Chem. Phys.* **56** 3086
    Waisman E and Lebowitz J L 1972 *J. Chem. Phys.* **56** 3093
    Blum L 1975 *Mol. Phys.* **30** 1529
[23] Valiskó M, Henderson D and Boda D 2004 *J. Phys. Chem.* B **108** 16548
[24] Hiroike K 1977 *Mol. Phys.* **33** 1195
[25] Blum L and Rosenfeld Y 1991 *J. Stat. Phys.* **63** 1177

[26] Press W H, Teukolsky S A, Vetterling W T and Flannery B P 1992 *Numerical Recipes in C: The Art of Scientific Computing* 2nd edn (Cambridge: Cambridge University Press)
[27] Donnan F G 1911 *Z. Elektrochem.* **17** 572
[28] Helfferich F 1962 *Ion Exchange* (New York: McGraw-Hill)
[29] Boda D, Chan K-Y and Henderson D 1998 *J. Chem. Phys.* **109** 7362
[30] Valleau J P and Torrie G M 1982 *J. Chem. Phys.* **76** 4623
[31] Shannon R D and Prewitt C T 1969 *Acta Crystallogr.* B **25** 925
[32] Bhuiyan L B, Blum L and Henderson D 1983 *J. Chem. Phys.* **78** 442
[33] Valleau J P and Torrie G M 1984 *J. Chem. Phys.* **81** 6291
[34] Torrie G M, Valleau J P and Outhwaite C W 1984 *J. Chem. Phys.* **81** 6296
[35] Martin Ph A 1988 *Rev. Mod. Phys.* **60** 1075
[36] Henderson D and Blum L 1978 *J. Chem. Phys.* **69** 5441
     Henderson D, Blum L and Lebowitz J L 1979 *J. Electroanal. Chem.* **102** 315
[37] Salacuse J J and Stell G 1982 *J. Chem. Phys.* **77** 3714
[38] Blum L 1980 *J. Stat. Phys.* **22** 661